Journal of Colloid and Interface Science 410 (2013) 1–10

Contents lists available at ScienceDirect

Journal of Colloid and Interface Science

www.elsevier.com/locate/jcis

Editor's Choice

Ordered gold nanoparticle arrays on glass and their characterization

Jie Yuan [a,b], Akram Hajebifard [c], Christeen George [a,b], Pierre Berini [c,d,*], Shan Zou [a,*]

[a] National Research Council of Canada, 100 Sussex Drive, Ottawa, Ontario K1A 0R6, Canada
[b] Department of Chemical and Biological Engineering, University of Ottawa, 161 Louis Pasteur, Ottawa, Ontario K1N 6N5, Canada
[c] Department of Physics, University of Ottawa, 150 Louis Pasteur, Ottawa, Ontario K1N 6N5, Canada
[d] School of Electrical Engineering and Computer Science, University of Ottawa, 800 King Edward, Ottawa, Ontario K1N 6N5, Canada

ARTICLE INFO

Article history:
Received 16 May 2013
Accepted 29 July 2013
Available online 12 August 2013

Keywords:
Gold nanoparticles (AuNPs)
Localized surface plasmon resonance (LSPR)
Self-assembly
Diblock copolymer
Seeding growth

ABSTRACT

Using self-assembly of block copolymer micelle loaded metal precursors, combined with a seeding growth route, we have developed a novel approach to create ordered metal nanoparticle (NP) arrays of controllable size over large areas (~80 mm^2) on solid substrates. Atomic force microscopy (AFM), UV–Vis extinction spectrophotometry, and theoretical simulations were systematically carried out to determine the size and pattern of NP arrays, and locate the localized surface plasmon resonance (LSPR) peak. By tuning the molar ratios of precursors, hexagonal arrays of AuNPs of mean heights of 5.2 ± 0.6 nm, 8.3 ± 1.7 nm, and 10.0 ± 2.1 nm were obtained by self-assembly of poly(styrene-*b*-2-vinyl pyridine) micelle-loaded gold salt on glass. Further seeding growth was then used to enlarge the AuNPs to heights of 25.7 and 33 nm and decrease the edge-to-edge inter-particle spacing. The optical response of AuNP arrays was determined by measuring and computing their absorbance spectra as a function of the cover medium refractive index over the range from 1 to 1.55; the measured spectra agree very well with the computations. The resonance wavelength red-shifts as the medium refractive index increases and the bulk sensitivity of the arrays increases with increasing AuNP size. When the edge-to-edge inter-particle spacing decreased to ~50 nm, coupling of adjacent AuNPs became apparent, as a shoulder which developed in the spectra. Also, the AuNPs were found to be embedded in the substrate glass by about ~20–30%, as determined by comparing the experimental and computed bulk sensitivities. The fabrication technique devised is suitable for low-cost mass-manufacturing of large area arrays of ordered high-quality AuNPs on a substrate for biosensor or other applications.

1. Introduction

The unique chemical, optical and electro-kinetic properties of gold nanoparticles (AuNPs), which are size- and shape-dependent, have been widely used in catalysts, solar energy harvesting, and sensing applications [1–5]. Although e-beam lithography or focused ion beam milling are commonly used to fabricate metallic nano-structures, the serial nature of these processes and their high costs are limiting. There is a pressing need for controlled solution-based nanoparticle fabrication methods applicable to large-area samples or substrates. Efforts have been expended in this direction but it remains challenging to create ordered metal NP arrays of controlled particle size and controlled spacing between particles. Using alkyl chain length (ligand-) controlled AuNP spacing, Lin and others have demonstrated the possibility to prepare AuNP super-lattices by controlling solvent evaporation [6–8]. However, this approach limits the spacing of AuNPs to ~3 nm due to difficulties in the synthesis of longer alkyl chain lengths [9]. DNA-based routes extended the AuNP spacing to 20 nm [10–16], but unfortunately, it is difficult to produce a continuous super-lattice sheet of AuNPs over a large area [12,16]. Möller et al. introduced the method of using diblock copolymer micelles to load metal precursors and form NP arrays on solid supports [17]. For example, $AuCl_4^-$ ions bind tightly to protonated pyridine units in the core of micelles so that the micelle structure served as nanoreactors and carriers of AuNPs [4,17–26]. This solution-based approach can yield NPs of uniform size (narrow size distribution), and is a simple and cost-friendly NP fabrication method [18,23,27].

Localized surface plasmon resonances (LSPRs) are charge density oscillations on metal NPs excited by light. They are sensitive to the optical properties of the surrounding environment. Metal NPs can scatter or absorb incident light. Extinction, the summation of absorption and scattering, is an optical property that characterizes metal NPs, particularly extinction spectra which reveal the location of LSPRs. According to the Mie theory [28], for metal NPs with a

* Corresponding authors at: School of Electrical Engineering and Computer Science, University of Ottawa, 800 King Edward, Ottawa, Ontario K1N 6N5, Canada. (P. Berini), National Research Council of Canada, 100 Sussex Drive, Ottawa, Ontario K1A 0R6, Canada (S. Zuo).

E-mail addresses: berini@eecs.uottawa.ca (P. Berini), shan.zou@nrc-cnrc.gc.ca (S. Zou).

0021-9797/$ - see front matter Crown Copyright © 2013 Published by Elsevier Inc. All rights reserved.
http://dx.doi.org/10.1016/j.jcis.2013.07.070

diameter much smaller than the exciting wavelength, the extinction, absorption and scattering cross-sections are given by [29]

$$c_{ext} = c_{abs} + c_{scat} \tag{1}$$

$$c_{abs} = k\mathrm{Im}(\alpha) = 4\pi R^3 \left(\frac{2\pi}{\lambda_0}\right) \left(\frac{3\varepsilon_2 \varepsilon_d^{3/2}}{|\varepsilon_1 + 2\varepsilon_d|^2 + \varepsilon_2^2}\right) \tag{2}$$

$$C_{scat} = \frac{1}{6\pi} k^4 |\alpha|^2 = \frac{8\pi R^6}{3} \left(\frac{2\pi}{\lambda_0}\right)^4 \varepsilon_d^2 \left(\frac{|\varepsilon_1 - \varepsilon_d|^2 + \varepsilon_2^2}{|\varepsilon_1 + 2\varepsilon_d|^2 + \varepsilon_2^2}\right) \tag{3}$$

$$\alpha = 4\pi R^3 \left(\frac{\varepsilon_m - \varepsilon_d}{\varepsilon_m + 2\varepsilon_d}\right) \tag{4}$$

where k is the wavenumber of the incident light, λ_0 is the free-space wavelength, R is the radius of the nanoparticle, ε_d is the dielectric constant of the surrounding medium, and $\varepsilon_m = \varepsilon_1 + i\varepsilon_2$ is the dielectric constant of the metal ($e^{-j\omega t}$ time-harmonic form implied). For a good plasmonic metal ($\varepsilon_2 \ll \varepsilon_1$) the extinction is largest at the wavelength where $\varepsilon_1 = -2\varepsilon_d, k = 2\pi\sqrt{\varepsilon_d}/\lambda_0$ for the case of the dipolar (bright) LSPR; we denote this wavelength as λ_{LSPR}. While λ_{LSPR} is mainly determined by the real part of the metal dielectric constant, the strength and width of theextinction, absorption and scattering spectra are determined mainly by the imaginary part of the dielectric constant, see Eqs. (1)–(3). For small NPs of diameter in the range of 10–30 nm, absorption dominates [30,31].

Several key factors are essential in characterizing metal NP arrays. First of all, λ_{LSPR} depends on the refractive index of the NP's surrounding medium, including the substrate, cover medium and any adsorbed species [1,3,32–39]. Secondly, when two or several AuNPs are deposited closely enough, inter-particle coupling is not negligible [40–46]. Depending on the orientation of AuNP arrays, the LSPR is polarization sensitive, and both red-shifts and blue-shifts can be achieved with increasing cover index [42]. Lastly, bandstructure effects can become more prevalent in the optical properties of AuNPs if they can be organized on the atomic scale [47]. In general, most of these characteristics can be enhanced significantly and utilized effectively if the AuNPs are organized in accurate and organized arrays [48].

Here, we report a simple fabrication method to generate hexagonal ordered AuNP arrays on glass cover slip substrates using self-assembly combined with seeding growth approach. As shown in Scheme 1, hexagonal patterned gold salt loaded poly(styrene-*b*-2-vinyl pyridine) (PS-*b*-P2VP) micelles are spin-coated on substrates, and the polymer shell is removed by oxygen plasma etching. Arrays of AuNPs with 5 to 10 nm in size were created on glass substrates forming "seeds", from which larger AuNPs were grown chemically. Series of AuNP sizes with controlled inter-particle spacing were obtained over large areas on glass substrates. The absorbance spectra of AuNP arrays on glass were characterized by UV–Vis spectroscopy. The influence of size, inter-particle spacing, surrounding permittivity (substrate and cover medium), and AuNP embedding ratio into the substrate are discussed. Also, the influence of the ionic strength and charge density of the micelle solution were considered.

2. Materials and methods

2.1. Chemicals

Diblock copolymer poly(styrene(48.5k)-*b*-2-vinyl pyridine(70k)) (PS-*b*-P2VP, Polymer Source Inc., Montreal, QC, Canada) was used as purchased. Gold(III) chloride hydrate (99.999%) ($HAuCl_4$) and hydroxylamine hydrochloride ($NH_2OH{\cdot}HCl$) were both purchased from Sigma–Aldrich Canada Ltd. (Oakville, ON, Canada), and used as received. 25 mm (78.5 mm^2) premium glass cover slip substrates were purchased from Fisher Scientific (Ottawa, ON, Canada). 45 × 12.5 × 3.5 mm^3 quartz cuvettes were purchased from Hellma Canada Ltd. (Concord, ON, Canada). HPLC grade methanol, dichloromethane, heptane, 99% ethanol, chloroform and *o*-dichlorobenze were purchased from EMD Chemicals Inc. (Gibbstown, NJ, USA), Greenfield Ethanol Inc. (Brampton, ON, Canada), Caledon Laboratories Ltd. (Georgetown, ON, Canada) and Sigma–Aldrich Inc. (St. Louis, MO, USA). ACS grade toluene (Fisher Scientific, Fair Lawn, NJ, USA) was purified using an Innovative Technology Pure Solv. Device (activated alumina column containing a copper catalyst and molecular sieves). Milli-Q water deionized to a resistivity of 18 MΩ cm was used in all of the experiments.

2.2. Combined self-assembly and seeding growth methods

Patterned AuNP arrays on glass cover slips were prepared by the self-assembly of diblock copolymer micelle loaded gold salt [17,25,26,48,49]. Briefly, 5 mg/mL diblock copolymer micelle solution was prepared in dry toluene by vigorous stirring. Gold precursor ($HAuCl_4$) was added to the micelle solution at a molar ratio of 0.1, 0.2, 0.3, 0.4 and 0.5 per pyridine unit. The gold loaded micelle

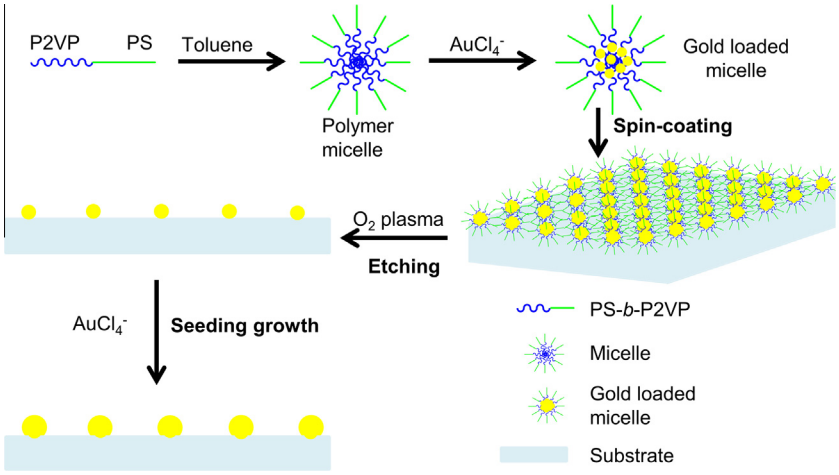

Scheme 1. Processes of forming ordered hexagonal AuNP arrays on glass substrates: combining the self-assembly of diblock copolymer micelle loaded gold precursors with the seeding growth method.

solution was stirred overnight and spin-coated on clean glass cover slips at 2000 rpm (SPIN COATER, Chemat Scientific, Northridge. CA, USA). The polymer was removed by 15 min treatment in an oxygen plasma etcher (PlannerEcher IIA, Technics Inc., San Jose, CA). Hexagonal patterned AuNP arrays were formed and may be partially embedded into the glass cover slip substrates [48]. The ordered AuNP arrays served as seeds for further seeding growth processes [50–58]. The pre-seeded samples were put in a growing solution with 0.24 mM gold precursor in a container. 5 mM hydroxylamine hydrochloride (NH_2OH) solution was dropped into the container with pre-seeded AuNP array on glass at 1 drop per second until the final concentration reached 0.5 mM. After 15 and 30 min, a homogenous cherry-red film appeared on the side of the glass slide bearing the AuNP seed array. The other side of the glass was covered by tape in order to avoid $AuCl_4^-$ stains. The samples were washed thoroughly with MQ water. By controlling the growth time and the concentration of the growth solution, the AuNP size and edge-to-edge inter-particle spacing are controlled.

2.3. Size measurement of gold precursor loaded PS-b-P2VP micelles in toluene

The diblock copolymer micelle diameters were evaluated by dynamic light scattering (DLS) (Nano Zetasizer, Malven Instrument Ltd, Worcestershire, United Kingdom). The sample was diluted to 0.1 mg/mL in toluene and filled in a PSC115-Glass cuvette of square aperture. All of the data were obtained at 25 °C.

2.4. Characterization of patterned AuNP arrays on glass

The height and inter-particle spacing of patterned AuNP arrays on glass were measured by an AFM (Nanowizard II BioAFM, JPK Instruments, Berlin, Germany) mounted on an Olympus IX81 inverted confocal microscope. Silicon cantilevers and tips (NSC14, MikroMasch, Estonia) were used to image all samples in intermittent contact mode. At least five locations on each sample were tested. Absorbance spectra measurements were carried out using a Varian Cary 5000 UV–VIS–NIR spectrometer (Varian Inc., AC, USA). For each measurement, the AuNP arrays on glass were immersed in each solvent sequentially while the surface of the AuNP arrays was kept perpendicular to the optical source. Multiple measurements were taken for each sample to ensure the reproducibility of the measurements. The absorbance spectrum of the AuNP arrays on glass was measured in each solvent in turn commencing with the solvent having the lowest refractive index. After each measurement, the substrate and the cuvette were rinsed in turn with methanol, ethanol and water, and then dried with nitrogen. This step was repeated several times to completely remove the previous solvent.

Two sets of solvents with different refractive index ranges were chosen. One set of six solvents provides refractive indices from 1.3284 to 1.4458, as listed in Table 1. The other set of six solvents were prepared by mixing toluene and *o*-dichlorobenzene at different volume ratios (Table 1). The refractive index of the toluene/*o*-dichlorobenzene binary mixture was estimated via Eq. (5) and all solvents were verified by prism-coupling techniques using a Metricon Model 2010 (Metricon Corporation, Pennington, NJ, USA).

$$n_{mix} = \frac{n_{D\text{-}Toluene} \times V_{Toluene} + n_{D\text{-}Dichlorobenzene} \times V_{Dichlorobenzene}}{V_{Toluene} + V_{Dichlorobenzene}} \quad (5)$$

The differences between the estimated values (n_D) and the measured values for all solvents (n_D^*) in Table 1 were less than 0.4%. Thus, the refractive index of the toluene/*o*-dichlorobenzene binary mixture was properly evaluated by Eq. (5). The stability of AuNP arrays on glass was verified in various solvents, such as ethanol (3 days), water (7 days), detergent aqueous solution (1 day), dichloromethane (3 h), piranha solution (H_2O_2(30%):H_2SO_4(97%) 1:4(vol), 5 min), and saturated potassium hydroxide in ethanol (15 wt%, 5 min). The arrays remained stable for further experiments.

Table 1
Refractive indices of toluene/o-dichlorobenzene binary mixtures and six other solvents used.

Toluene and o-Dichlorobenzene mixture	Refractive index of binary mixture (n_D)	Refractive index of binary mixture (n_D^*)
T/D 1:0	1.4969	1.49112
T/D 3:7	1.5133	1.51094
T/D 1:1	1.5242	1.52198
T/D 7:3	1.5351	1.53541
T/D 1:9	1.5460	1.54191
T/D 0:1	1.5514	1.54580
Solvents	**Refractive index (n_D)**	**Refractive index (n_D*)**
Methanol	1.3284	1.32598
Water	1.3330	1.32724
Ethanol	1.3614	1.35922
Heptane	1.3876	1.38781
Dichloromethane	1.4241	1.41850
Chloroform	1.4458	1.44265

Note: The n_D was estimated by assuming that the refractive index of the binary mixture is proportional to the volume ratio of the two components for the toluene and *o*-dichlorobenzene binary mixture. For solvents, it was evaluated by the ratio of the velocity of light (sodium D line) in air to the velocity of light in the solvent at 20 °C (provided by Burdick & Jackson). The n_D^* was experimental measurement by using Metricon Model 2010. T/D represents the volume ratio of the two components in the mixture.

2.5. Computations

The calculations were carried out using the RF module of COMSOL finite element software. The modeling was defined as following: the unit cell is illuminated by a plane-polarized electromagnetic wave from the top (Scheme 2), and absorbance is calculated as the optical response of the sample. An x-polarized wave strikes the unit cell and propagates through the medium along the unit cell. A surface integral on the *z* component of the time averaged pointing vector is used to calculate transmittance and then absorbance. The following equation is applied for the calculation of the absorbance (as measured):

$$A = -log\left(\frac{T}{T_0}\right) \quad (6)$$

where A is the absorbance, and T and T_0 are used to denote the transmittance with and without the nanoparticle in the unit cell, respectively. The absorbance is computed over the spectral range corresponding to a free space wavelength of 400–700 nm.

Computations have been done for AuNPs with a height of 10 nm, and 25.7 nm. The 33 nm one was modeled as an oblate spheroid having a ratio of major to minor axes of 1.06. The longitudinal diameter along the glass-superstrate interface is 35 nm and the transverse one is 33 nm. The edge-to-edge inter-particle spacing used was 52, 46 and 29 nm, for the 10, 25.7 and 33 nm NPs, respectively. In all cases, an AuNP array is assumed to involve an infinite number of particles with the same shape and center to center inter-particle distance. Since the geometrical properties of the NPs fluctuate particle to particle, the averaged geometrical properties of the experimental sample were chosen. AuNPs fabricated on the glass have a quasi-hexagonal pattern, as shown in Scheme 2(A) and (D). This kind of pattern can be made by repeating a parallelogram-shape unit cell with equal sides representing center to center inter-particle spacing, as shown in Scheme 2(A).

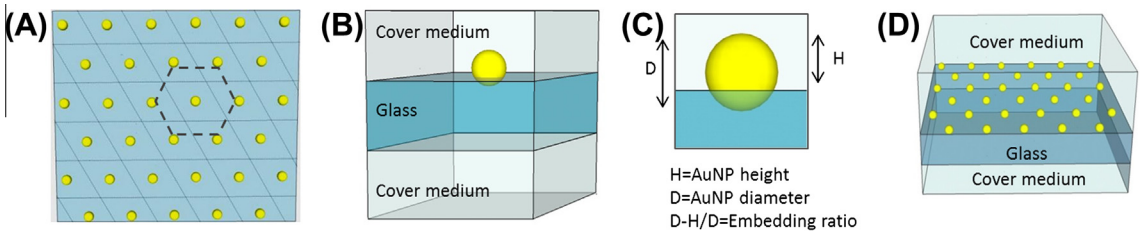

Scheme 2. (A) Model of an AuNP array fabricated on a glass substrate; the array pattern is hexagonal. (B) Simulated parallelepiped unit cell includes a glass-supported AuNP bounded by cover media. (C) An AuNP embedded into the surface of the glass slide. (D) AuNP arrays on a glass substrate exhibited a quasi-hexagonal pattern.

To take advantage of the structural symmetry, only one unit cell including one NP is modeled, as shown in Scheme 2(B). Scattering boundary conditions are applied to the top and bottom of the unit cell to define an incident wave with boundaries having no physical reflections into the cell. Periodic boundary conditions have been applied to the rest of the boundaries.

Different mesh densities have been tested to assess convergence of the analysis. The optimum discretization was chosen to be 0.8 nm within the NP domain and in its vicinity, and 3 nm within the rest of the domain. Since the skin depth for gold (~25 nm) over the spectral range of interest is of the order of the particle diameter, the mesh density within the entire gold domain was taken as 0.8 nm.

2.6. Calculated optical properties

The optical properties of the materials used in the computations were taken as the frequency-dependent complex refractive index (permittivity) measured over the wavelengths of interest for glass [59], gold [60,61], and some of our solvents [62–64], such as methanol, water, ethanol, heptane, chloroform and toluene. Cubic spline interpolation functions were applied to determine the materials' refractive index at specific wavelengths of interest where data are not available. For other solvents a wavelength-independent refractive index at the sodium D line (λ = 589 nm) was chosen for the whole spectra range. Refractive index values of 1.4241, 1.5514, 1.5132, 1.5241, 1.5351, and 1.5459 were used for dichloromethane, o-dichlorobenzene, T/D 3:7, T/D 1:1, T/D 7:3, T/D 1:9 respectively.

3. Results and discussion

3.1. Self-assembly controlled formation of AuNP seed arrays

Atomic force microscopy (AFM) height images of representative AuNP seed arrays formed with 0.1, 0.2 and 0.5 mol ratio of gold precursor per pyridine unit are shown in Fig. 1. Correspondingly, the mean heights of AuNPs were 5.2 ± 0.6, 8.3 ± 1.7, and 10.0 ± 2.1 nm, respectively. Fast Fourier transformed (FFT) images are shown as insets to the AFM topography images in Fig. 1. The AFM height images although limited in area are typical of the distribution of particles over the full area of the glass substrate (~80 mm^2). Ordered hexagonal patterns were obtained when the standard deviation of height distribution was controlled to within ±0.6 nm; as the deviation increased, the hexagonal patterns degraded slightly (as shown in Fig. 1(B) and (C)). When the gold precursor loading ratio (in short, the loading ratio) increased, the center-to-center distance (D) varied. The distance initially increased from 80 ± 8 to 88 ± 9 nm as the loading ratio increased from 0.1 to 0.2 mol/pyridine unit (Fig. 1(A) and (B)), then as the loading ratio increased to 0.5 mol/pyridine unit, the D decreased to 62 ± 11 nm as shown in Fig. 1(C).

3.2. Micelle sizes and inter-particle spacings of AuNPs

In order to understand the non-linear relation between the inter-particle spacing and the loading ratio per pyridine unit, the diameter of PS-P2VP micelles in toluene was evaluated by dynamic light scattering (DLS). Fig. 2 shows that the micelle diameter was 83 nm with the loading ratio of 0.1 mol per pyridine unit, then expanded to 91 nm as the loading ratio increased to 0.2 mol per pyridine unit, and reached a maximum of 94 nm as the loading ratio increased to 0.3. However, further increasing the loading ratio led to a decrease in micelle diameter; as the ratio increased to 0.4 and 0.5, the micelle diameter decreased to 84 and 67 nm, respectively. This finding is partially supported by other studies which showed that increasing the loading ratio would only cause a marginal expansion of the micelle [23]. We propose the following that may lead to micelle shrinkage at a high loading ratio.

Once the gold precursors accumulate in the core area of micelles where is enriched in P2VP blocks, the salt will alter the interaction between the polymer chains locally, as well as between the polymer and solvent. In toluene, the accumulation of gold salt enhances the unfavorable interaction between P2VP core and the solvent (thus with the PS corona), resulting in collapses of PS chains and the shrunk of corona (PS) thickness. At the same time, due to the favorable interaction between the P2VP blocks and the gold salt, the core of micelles may expand. At a low loading ratio, the influence of the gold precursor on the PS corona is not as significant as on the P2VP, such that the micelle diameter expands slightly. When further increasing the loading ratio the core–shell structure changes accordingly. When micelles with larger core covered by thinner layer of PS shell were formed, their structures are not as stable as the micelles with lower loading ratios of gold precursors.

In Fig. 2, the micelle diameters measured in toluene by DLS coincides with the AuNP inter-particle spacing on the substrate. This is not surprising because the gold-loaded micelles in solution were spun on the substrate surface and the inter-particle spacing is dominantly controlled by the micelle diameter. During solvent evaporation, the surface tension causes a monolayer of micelles formed onto the substrate surface, thus preserving the inter-particle spacing after the sample was dried.

Absorbance spectra of AuNP seed arrays on glass with the mean height of 10.0 ± 2.1 nm were measured for cover media (solutions) of refractive index ranging from 1 to 1.5514, as shown in Fig. 3(A). The spectra were offset along the y-axis for clarity except for the one measured in air. The λ_{LSPR} is observed to increase with the cover medium refractive index, i.e., the resonances red-shift with increasing index. There was no shoulder apparent in the absorbance spectra; thus, coupling between different AuNPs was negligible (the inter-particle spacing here was 62 ± 11 nm) [41,65]. Arrays of seed AuNPs of different sizes are compared in Fig. 3(B). The λ_{LSPR} of the arrays, measured with a cover medium of refractive index 1.3876, shifted from 524 to 527 nm, then to 532 nm, as the AuNP mean heights increased from 5.2 ± 0.6 to 8.3 ± 1.7 nm and

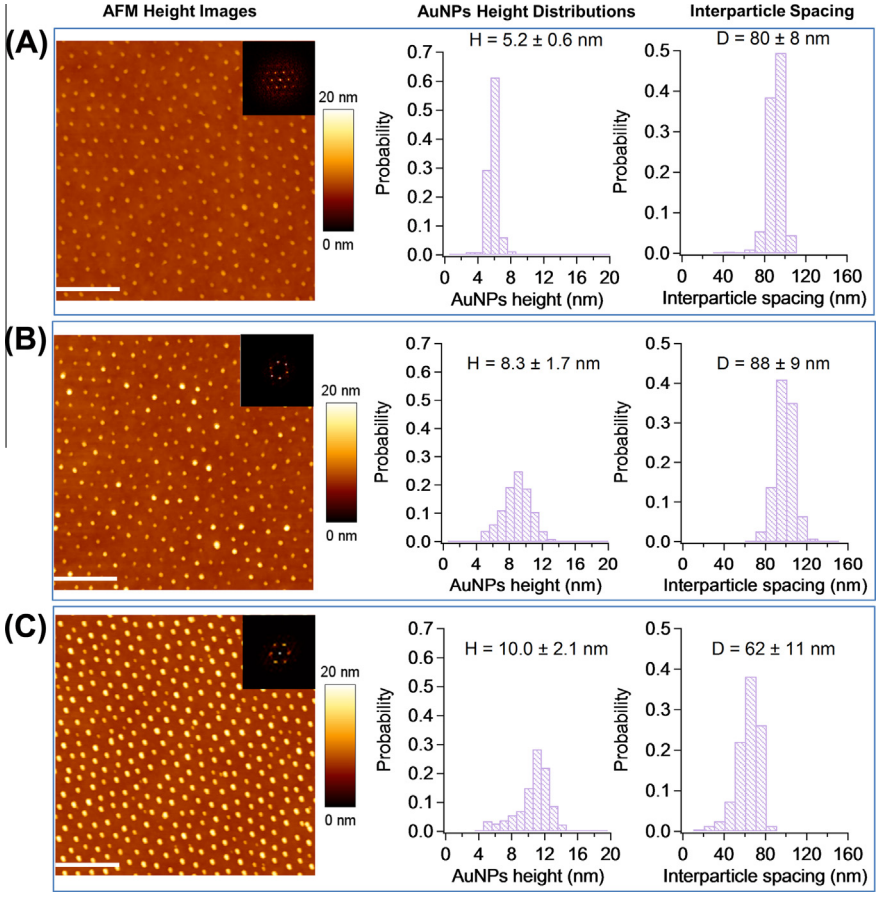

Fig. 1. Representative patterned AuNP (seed) arrays with different heights and center-to-center distances of the nearest neighbor. AuNP array samples with height distribution (H) and center to center distance (D) determined from AFM topography images: H of 5.2 ± 0.6 nm and D of 80 ± 8 nm (A); H of 8.3 ± 1.7 nm and D of 88 ± 9 nm (B); H of 10.0 ± 2.1 nm and D of 62 ± 11 nm (C). Insets to AFM height images are the fast Fourier transformed images of the corresponding height images. Scale bars on AFM images are 350 nm; the numbers of counted particles in each panel are in the order of 350–800.

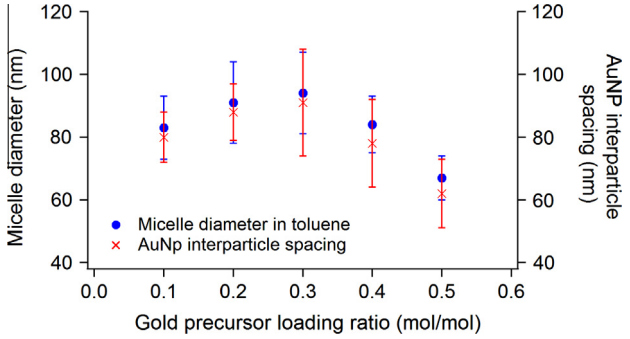

Fig. 2. Comparison between micelle diameters in toluene and the inter-particle spacings of AuNPs on glass.

then to 10.0 ± 2.1 nm, respectively. Thus λ_{LSPR} is sensitive to AuNP size (height), as well as to the cover medium refractive index [36].

3.3. Seeding growth to enlarge the size of AuNPs on hexagonal seed arrays

In order to better understand the influences of AuNP size, inter-particle spacing and surrounding medium refractive index, absorbance measurements were obtained on enlarged AuNP arrays prepared using our self-assembly and seeding growth approaches. Samples were prepared by using AuNP seed arrays with the mean height of 10 nm and center-to-center inter-particle spacing of 62 nm followed by chemically seeding growth. As observed from the AFM images in Fig. 4, the grown AuNP mean heights are 25.7 ± 2.7 nm (A), and 33.0 ± 4.4 nm (B) and the edge-to-edge inter-particle spacings are 46 and 29 nm, respectively.

λ_{LSPR} increases more with increasing cover medium refractive index for the samples with larger AuNPs. In addition, as the AuNP size increases, and the edge-to-edge inter-particle spacing decreases, coupling between AuNPs becomes observable in the measured absorbance: as noted from Fig. 4(B), in addition to the main λ_{LSPR}, a clear shoulder appears at a longer wavelength (~650–670 nm) in the absorbance spectrum for the case of air as the cover medium (the inter-particle spacing is less than 5 times of the AuNP radius) [66]. Interestingly, when the cover medium refractive index increases, the shoulder disappears (in addition to red-shifting λ_{LSPR}), indicating weaker coupling between particles. It is known that λ_{LSPR} and particle coupling are highly depended on the refractive index of the medium [67]. In this case the fields are increasingly confined to the AuNPs as the medium refractive index increases leading to less coupling.

3.4. Computations

It is worth to notice that in Figs. 1 and 4, the applied forces (i.e., imaging parameters) were controlled at the minimum to preserve the AuNP patterns while the AFM tip was scanning across the samples. Surprisingly, when changing the imaging mode to contact mode and increasing the imaging setpoint values

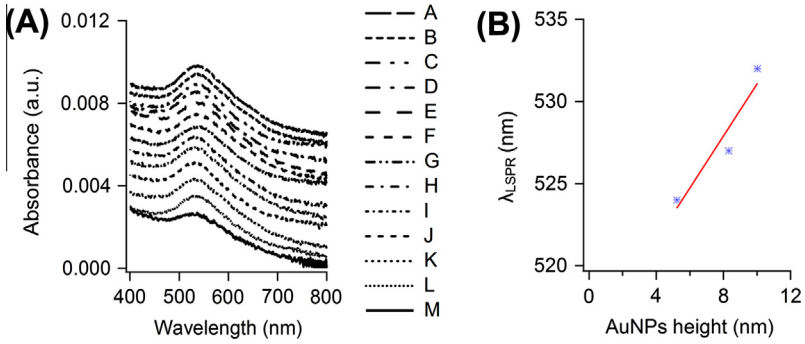

Fig. 3. (A) Measured absorbance spectra on representative AuNP (seed) arrays of height 10.0 ± 2.1 nm on glass for cover media (solutions) of refractive index ranging from 1.5514 to 1 (See Table 1 for details). A, *o*-dichlorobenzene; B, T/D 1:9; C, T/D 3:7; D, T/D 1:1; E, T/D 7:3; F, toluene; G, chloroform; H, dichloromethane; I, heptane; J, ethanol; K, MilliQ water; L, methanol; M, air. T/D represents the binary mixture of toluene and *o*-dichlorobenzene by volume ratio. Spectra are off-set along the y-axis for clarity by 0.0002 a.u. (B) λ_{LSPR} of AuNP seed arrays in heptane (n = 1.3876) showing a positive linear relation to AuNP heights.

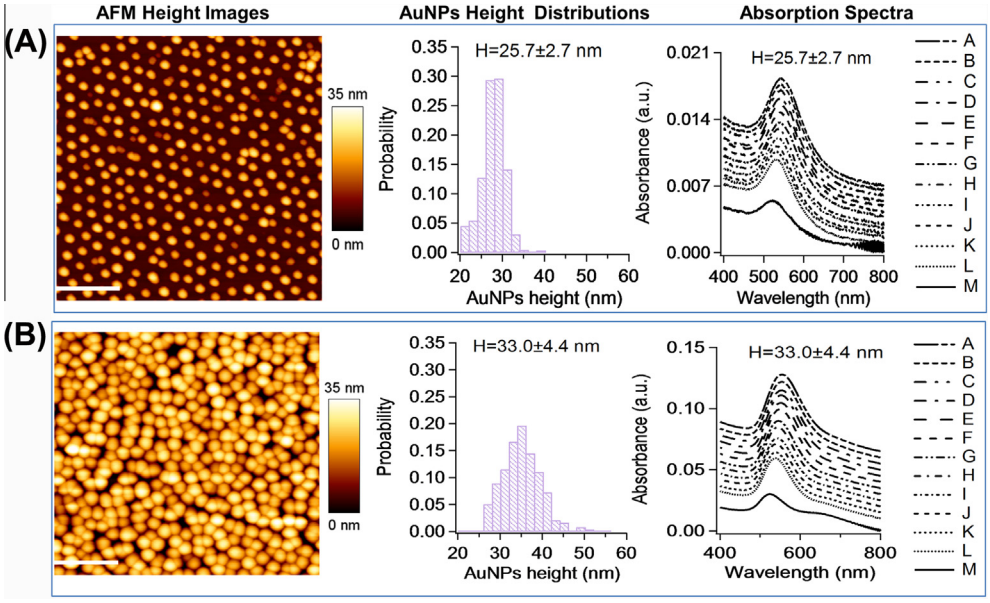

Fig. 4. Representative AuNP arrays of different heights after seeding growth and measured absorbance spectra for different cover media. (A) AuNP array with height distribution (H) of 25.7 ± 2.7 nm; (B) AuNP array with H of 33.0 ± 4.4 nm. The scale bars are 350 nm in the AFM images, and the numbers of counted particles in each panel are in the order of 350–800. Spectra are off-set along the y-axis for clarity by 0.0002 a.u. A, *o*-dichlorobenzene; B, T/D 1:9; C, T/D 3:7; D, T/D 1:1; E, T/D 7:3; F, toluene; G, chloroform; H, dichloromethane; I, heptane; J, ethanol; K, MilliQ water; L, methanol; M, air. T/D represents the binary mixture of toluene and o-dichlorobenzene by volume ratio (see Table 1 for details).

to applied forces of 15–20 nN, the hexagonal AuNP array patterns were retained after 7 days soaking in aqueous solution. The hexagonal patterns also survived from multiple peels of scotch tape. So it is reasonable to speculate that the particles are embedded slightly into the glass slide. Thus, absorbance computations for AuNPs on/embedded into glass cover slips were carried out to help understand and interpret the experimental results. The AuNP arrays form a quasi-hexagonal pattern made of a repeated parallelogram unit cell, as shown in Scheme 2. To take advantage of the structural symmetry, only one unit cell including one AuNP was modeled using periodic boundary conditions on lateral walls and absorbing boundary conditions above and below. Scheme 2(C) shows an AuNP embedded into the glass surface and defines the embedding ratio. The structure was excited by a plane wave incident from the top and the absorbance was computed (Scheme 2(D)).

As Boreman et al. [68] have shown, there is a combination of data from Palik [61] and Johnston and Christy [60] (JC) which forms the best set for nanostructures made of gold. In this set of data the imaginary part of the dielectric constant is taken from JC, and its real part taken as a mixture of data from JC and Palik. Palik's data is used over the spectral range of 400–500 nm, and JC's data is applied above 500 nm. In addition, the optical properties of gold were corrected for the nanoparticle sizes of interest (Fig. 5) [69,70]. Utilizing this set of data in the computations leads to a good agreement between numerical and experimental results in terms of λ_{LSPR}.

Fig. 5 illustrates how the optical properties of AuNPs depend on their radius. As seen in the plots $-Im\{\varepsilon_{Au}\}$, the negative imaginary part of the gold dielectric constant decreased with increased particle radius. However, $-Re\{\varepsilon_{Au}\}$, the negative real part of the gold dielectric constant, increases with particle radius. In addition, it is obvious from Fig. 5 that the optical properties of smaller AuNPs are more size-dependent than the bigger ones. This fact results in having broader experimental absorbance spectra than the computations for small AuNPs.

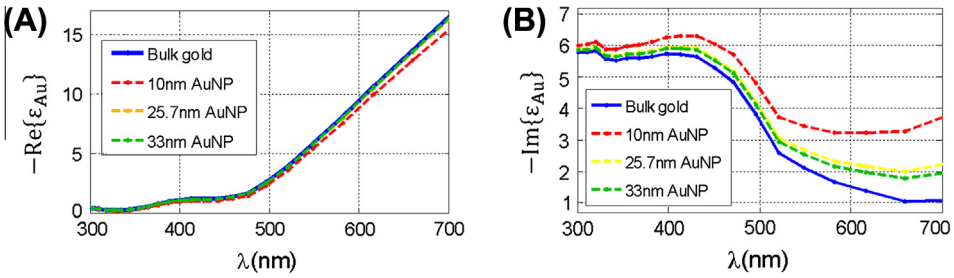

Fig. 5. Size-dependent real part (A) and imaginary part (B) of the gold dielectric constant.

Fig. 6(A)–(C) show the computed spectra of AuNP arrays with mean heights of 10, 25.7 and 33 nm, respectively, as the cover medium refractive index varied from 1 to 1.5514. The computations agree well with the experimental results as observed via comparisons with the measured spectra of Figs. 3 and 4, and as summarized in Fig. 6(D)–(F) which plot the measured and computed λ_{LSPR} versus the cover medium refractive index. A red shift from 521 to 539 nm for 10 nm AuNPs, from 522 to 544.5 nm for 25.7 nm AuNPs, and from 525.5 to 553 nm for 33 nm AuNPs, is achieved over the full range of indices. Thus, λ_{LSPR} is strongly dependent on the refractive index of the cover medium, which is a well-known characteristic of metal nanoparticles [35,69,71–74]. The origin of this dependence comes from the LSPR condition, $\varepsilon_1 = -2\varepsilon_d$. Since the negative real part of the dielectric constant of gold increases with wavelength in the visible range [60,61], an increase in the surrounding medium's dielectric constant causes λ_{LSPR} to red-shift. From Fig. 6(D)–(F) we also note that increasing the AuNP size and shrinking the inter-particle spacing red-shift λ_{LSPR} due to increasing electromagnetic retardation in larger particles [71,75]. Therefore, not only is λ_{LSPR} sensitive to the cover medium refractive index, but also to the AuNP size.

As noted from the spectra of Figs. 3 and 4 (measured) and Fig. 6(A)–(C) (computed), the peak absorbance increases with increasing cover medium refractive index. This is expected in part from Mie theory, as Eq. (2) shows that the absorption cross-section increases with the (homogeneous) background refractive index. This is also apparent from computations of the heat loss distribution for 10 nm AuNPs bounded by cover media of different refractive indices, revealing increasing heat loss with increasing index, see Fig. 7).

3.5. Optical properties of the AuNP arrays

As observed from the measurements (Figs. 3 and 4) and computations (Fig. 6), the absorbance peak also increases with AuNP size. This is consistent with the literature[76] and expected theoretically (Eqs. (2), (3)). In air, for 10 nm AuNP arrays, the measured absorbance peak is 2.65×10^{-3} (Fig. 2(A)); for 25.7 nm AuNP arrays, the absorbance peak increases to 5×10^{-3} (Fig. 4(A)); and for 33 nm AuNP arrays, the absorbance peak reaches 0.03 (Fig. 4(B)). This trend is verified in the computations (Fig. 6(A)–(C)), although the value of the peak absorbance agrees only to within a factor of ~3.

The distribution in inter-particle spacing and size of the AuNPs is thought to cause the discrepancy between the experimental and computed absorbance – the measured absorbance peaks are

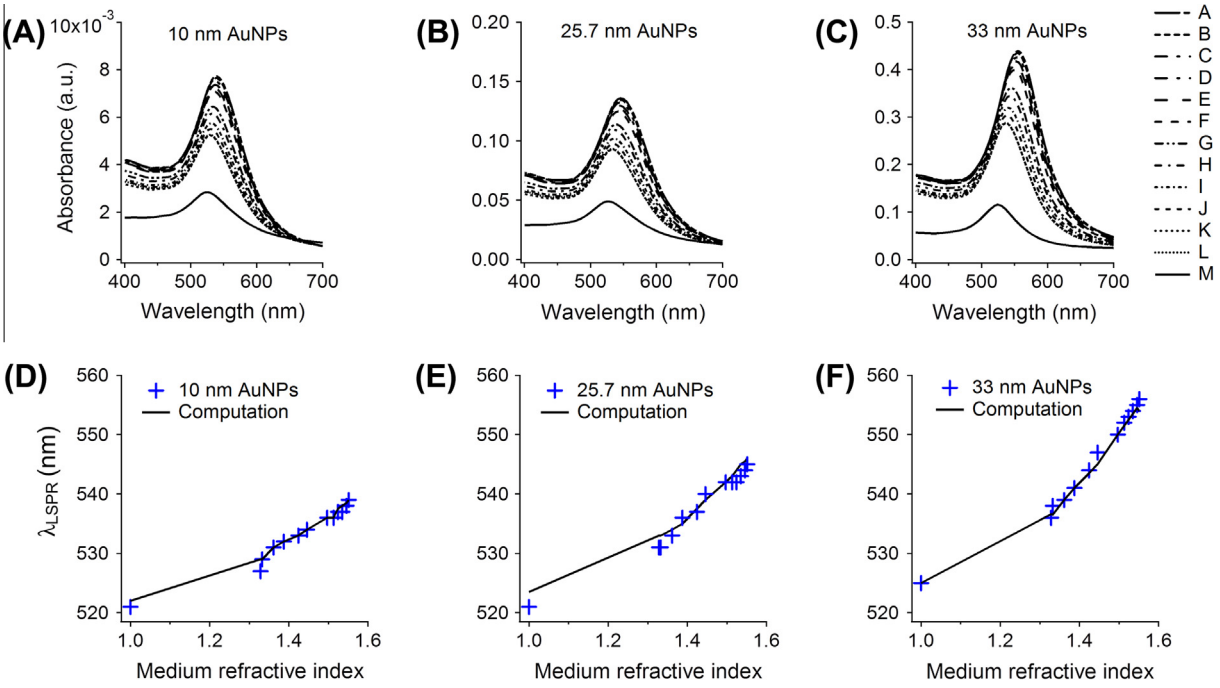

Fig. 6. (A)–(C): Computed absorbance spectra of AuNP arrays with mean heights of 10 nm (A), 25.7 nm (B) and 33 nm (C) for various cover media: A, *o*-dichlorobenzene; B, T/D 1:9; C, T/D 3:7; D, T/D 1:1; E, T/D 7:3; F, toluene; G, chloroform; H, dichloromethane; I, heptane; J, ethanol; K, MilliQ water; L, methanol; M, air. T/D represents the binary mixture of toluene and *o*-dichlorobenzene by volume ratio. An embedding ratio of 20% was assumed in these computations. (D)–(F) Experimental and computed λ_{LSPR} versus cover medium refractive index for AuNP arrays with mean heights of 10 nm (D), 25.7 nm (E), and 33 nm (F).

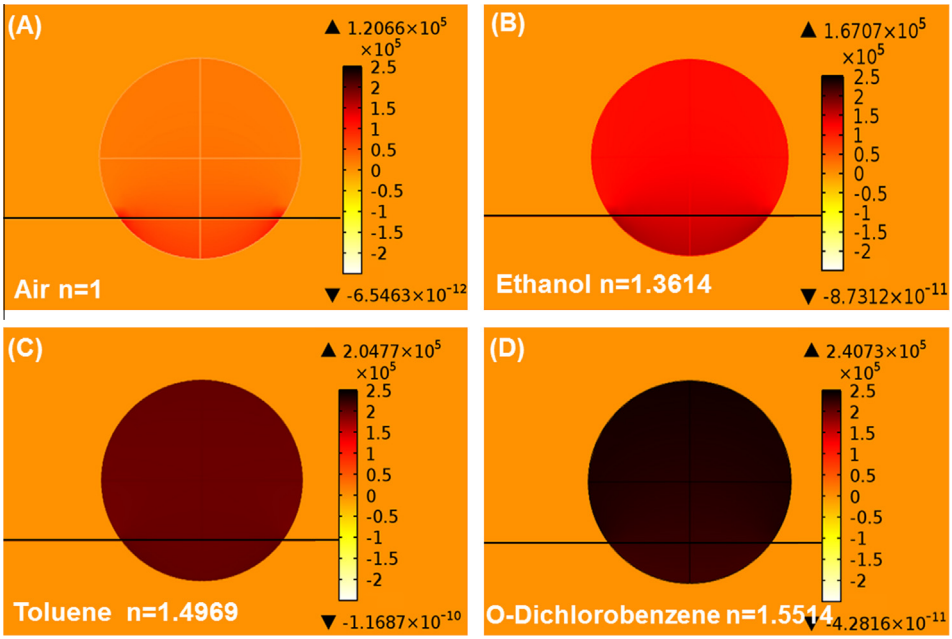

Fig. 7. Computed heat loss distribution at λ_{LSPR} for a 10 nm AuNP surrounded by (A) air, (B) ethanol, (C) toluene and (D) *o*-dichlorobenzene. Increasing cover medium refractive index leads to raising heat loss in AuNPs.

consistently lower than the computed ones. In the computations, the radius and spacing are invariant over the array as periodic boundary conditions are applied, whereas these quantities are distributed in the experimental samples (Figs. 1(C), 4(A) and (B)). The optical parameters of gold deviate from bulk values in very small particles (see Fig. 5), so the size distribution results in a distribution of optical parameters across the array. Because the largest deviations occur for the smallest diameters, the 10 nm AuNPs show the largest discrepancy between experimental and computed results. However, the deviations between the computed and measured λ_{LSPR} were no more than 1 nm, except for the case of water, which might be due to the influences of ionic strength and charge density which alter the LSPR fields.

Absorbance spectra of AuNPs on glass were affected by ion concentration, as shown in Fig. 8(A). MilliQ water and PBS buffer were served as the bulk surroundings without/with ions, respectively. In water, the λ_{LSPR} was at 529.4 nm; in PBS buffer, the λ_{LSPR} of the same sample was shifted to 533.3 nm. (PBS buffer contains 1.544 mM $[K^+]$, 157.881 mM $[Na^+]$, 1.544 mM $[H_2PO_4^-]$, and 2.709 mM $[HPO_4^{2-}]$). The refractive index is 1.33137 for MilliQ water and 1.33324 for PBS buffer. When the proton concentration is increased, which is represented by pH value of the solution, the positive charge density in solution cannot be negligible to electric field distribution of AuNPs. A patterned AuNP array on glass with a mean height of 25 nm was tested in PBS buffer solutions with different pH, as shown in Fig. 8(B) and (C). The correlation between the λ_{LSPR} position and proton concentration indicates that the λ_{LSPR} position is shifted to longer wavelength when the proton concentration is close to neutral. Herein, proton concentration has a negative effect of absorbance spectra. Also, this effect is diminished by the ion effect in our experiments. Hence, when AuNPs presented in a saline buffer surroundings, the overall behavior of the absorbance is still red-shift.

3.6. Bulk sensitivity

As the refractive index of the cover medium increases to values that are comparable with the index of the glass substrate, the LSPR fields become increasingly symmetrical, which leads to an increased bulk sensitivity for arrays with a cover medium of higher refractive index.

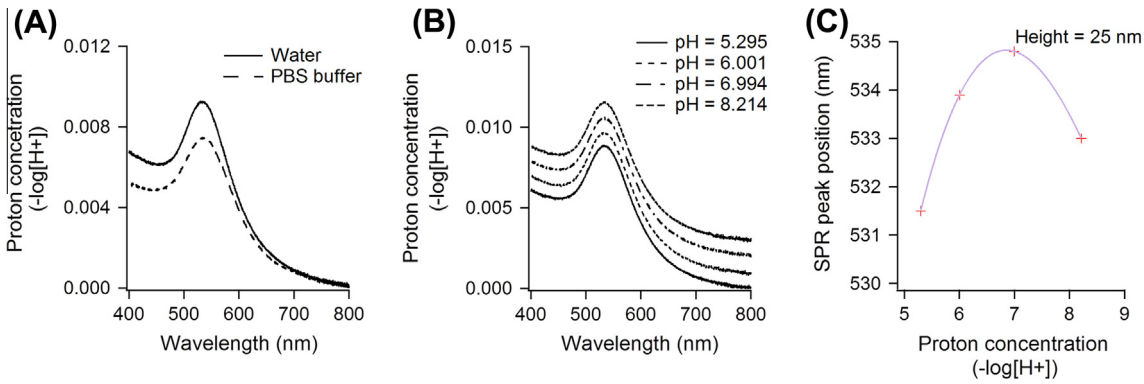

Fig. 8. Absorbance spectra of AuNPs on glass affected by ion concentration (A); proton concentration (B); and the correlation between λ_{LSPR} position and proton concentration in bulk surrounding (C).

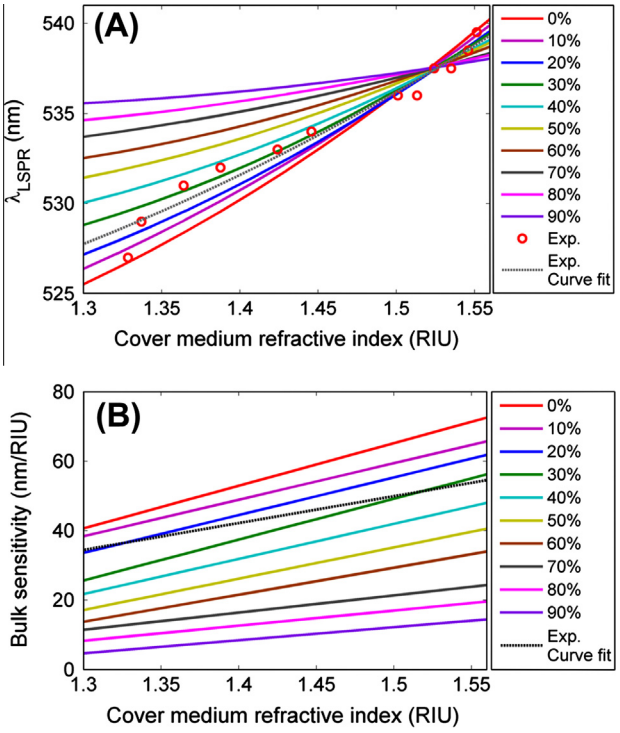

Fig. 9. (A) λ_{LSPR} and (B) bulk sensitivity versus cover medium refractive index for 10 nm AuNPs of different embedding ratios. The red circles and gray dashed curve correspond to the experimental results.

Comparing our λ_{LSPR} (Fig. 6(D)–(F)) to those of similar-sized AuNPs suspended in the same solvent [49,77,78] reveals that our λ_{LSPR} are ~10 nm larger. The reason for this is that our AuNPs are on (or embedded a few nanometers into) a glass surface, thus causing a distortion in the fields of the dipolar resonant mode when covered with a low-index medium – the fields are thus different from those of a suspension of AuNPs in a homogeneous medium. In this situation, ε_d in Eqs. (1)–(3) could be considered as an "effective" dielectric constant which may reasonably be assumed as the mean value of the glass and cover medium dielectric constants. Therefore, fulfillment of the LSPR condition, $\varepsilon_1 = -2\varepsilon_d$ in Eqs. (1)–(3), is achieved at a longer wavelength, explaining the red-shift in our λ_{LSPR} relative to other work [79].

From Fig. 6(D)–(F) we notice that as the AuNP height increases from 10 to 25.7 then to 33.0 nm, λ_{LSPR} red-shifts more with increasing cover medium refractive index. The sensitivity of λ_{LSPR} to the cover medium refractive index ($\Delta\lambda/\Delta n$) over the range of 1.3284–1.5514 is on average about 43.4, 54.4 and 85.0 nm/RIU for the 10, 25.7 and 33 nm arrays, respectively. Thus, the sensitivity is proportional to AuNP size.

Increasing the embedding ratio decreases the bulk sensitivity, as observed for the 10 nm AuNP array in Fig. 9. The more the AuNPs are embedded into the glass, the less their surfaces are exposed to the cover medium, resulting in less sensitivity. Comparing the computed with the experimental λ_{LSPR} and bulk sensitivities (Fig. 9) reveals that the AuNPs are embedded into the glass surface by ~20% to 30%.

The bulk sensitivity also depends on the cover medium refractive index, partly because the AuNPs are bounded asymmetrically (glass and cover medium). Fields penetrate more into the medium with the higher refractive index which is glass in this case. As the refractive index of the cover medium increases, approaching that of the glass, the fields become symmetrically distributed, penetrating more into the cover medium, as shown in Fig. 10. Distributions of the Ex field component on the resonance for 10 nm AuNPs bounded to glass below. Consequently, higher bulk sensitivity and a larger field enhancement are achieved in a higher refractive index cover medium.

4. Concluding remarks

In conclusion, we have presented a novel fabrication method for producing patterned AuNP arrays on large-area glass substrates by combining seeding growth with diblock copolymer self-assembly. The method provides a new approach to tune the AuNP size and edge-to-edge inter-particle spacing while preserving the AuNP ordering. Diblock copolymer self-assembly provided AuNP seeds with mean heights of 5.2 ± 0.6, 8.3 ± 1.7 and 10.0 ± 2.1 nm, and center-to-center inter-particle spacings of 80 ± 8, 88 ± 9 and 62 ± 11 nm by varying the molar ratio of the gold precursor to pyridine unit. The samples with 10.0 ± 2.1 nm AuNP seeds were treated by chemical growth methods to enlarge their sizes to mean heights of 25.7 ± 2.7 and 33.0 ± 4.4 nm, while simultaneously reducing the edge-to-edge inter-particle spacing to 37 and 29 nm, respectively. The properties of several AuNP arrays on glass were fully characterized, including their size, edge-to-edge inter-particle spacing, optical spectral properties and LSPR wavelength, bulk refractive index sensitivity, and embedding ratio. Optical modeling results agree well with the experimental results and allowed deduction of the embedding ratio of the AuNPs into the glass surface. The fabrication method is easy to apply and yields uniform, large-area (~80 mm^2), ordered arrays of AuNPs of controllable size and inter-particle spacing.

Acknowledgments

We thank Dr. Maohui Chen, Dr. Zygmunt Jakubek and Dr. Zhengfang Lu for technical supports, and Anthony Olivieri and Ewa Lisicka-Skrzek for assistance with the Metricon measurements. This work was partially supported by the National Sciences and Engineering Research Council (NSERC) of Canada through the Strategic Network BiopSys.

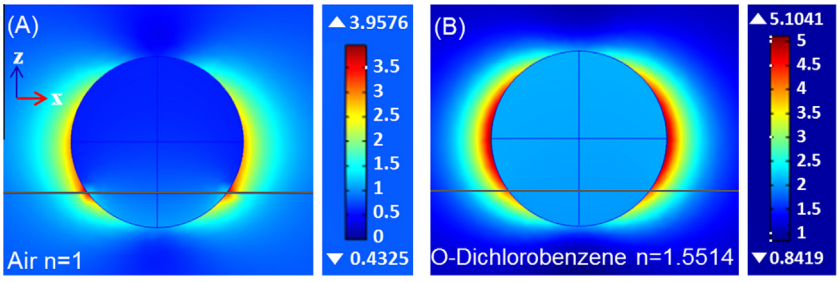

Fig. 10. Distribution of the Ex field component on resonance for 10 nm AuNPs bounded by glass below; (A) air, and (B) o-dichlorobenzene were set as the cover medium, respectively. An embedding ratio of 20% was assumed.

References

[1] K.C. Vernon, A.M. Funston, C. Novo, D.E. Gomez, P. Mulvaney, T.J. Davis, Nano Lett. 10 (2010) 2080.
[2] A. Lopatynskyi, O. Lopatynska, V. Chegel, Semicond. Phys. Quantum Electron. Optoelectron. 14 (2011) 114.
[3] T.J. Davis, D.E. Gomez, K.C. Vernon, Phys. Rev. B 81 (2010) 045432.
[4] D. Li, J.Y. Lee, D.H. Kim, J. Colloid Interface Sci. 354 (2011) 585.
[5] H.M. Kim, S.M. Jin, S.K. Lee, M.-G. Kim, Y.-B. Shin, Sensors 9 (2009) 2334.
[6] J. He, P. Kanjanaboos, N.L. Frazer, A. Weis, X.-M. Lin, H.M. Jaeger, Small 6 (2010) 1449.
[7] X.M. Lin, H.M. Jaeger, C.M. Sorensen, K.J. Klabunde, J. Phys. Chem. B 105 (2001) 3353.
[8] E. Rabani, D.R. Reichman, P.L. Geissler, L.E. Brus, Nature 426 (2003) 271.
[9] J.E. Martin, J.P. Wilcoxon, J. Odinek, P. Provencio, J. Phys. Chem. B 104 (2000) 9475.
[10] A.P. Alivisatos, K.P. Johnsson, X.G. Peng, T.E. Wilson, C.J. Loweth, M.P. Bruchez, P.G. Schultz, Nature 382 (1996) 609.
[11] W. Cheng, M.J. Campolongo, J.J. Cha, S.J. Tan, C.C. Umbach, D.A. Muller, D. Luo, Nat. Mater. 8 (2009) 519.
[12] C.A. Mirkin, R.L. Letsinger, R.C. Mucic, J.J. Storhoff, Nature 382 (1996) 607.
[13] D. Nykypanchuk, M.M. Maye, D. van der Lelie, O. Gang, Nature 451 (2008) 549.
[14] S.Y. Park, A.K.R. Lytton-Jean, B. Lee, S. Weigand, G.C. Schatz, C.A. Mirkin, Nature 451 (2008) 553.
[15] J.P. Zhang, Y. Liu, Y.G. Ke, H. Yan, Nano Lett. 6 (2006) 248.
[16] J. Zheng, P.E. Constantinou, C. Micheel, A.P. Alivisatos, R.A. Kiehl, N.C. Seeman, Nano Lett. 6 (2006) 1502.
[17] J.P. Spatz, A. Roescher, M. Moller, Adv. Mater. 8 (1996) 337.
[18] R. Glass, M. Moller, J.P. Spatz, Nanotechnology 14 (2003) 1153.
[19] J.P. Spatz, T. Herzog, S. Mossmer, P. Ziemann, M. Moller, Adv. Mater. 11 (1999) 149.
[20] J.P. Spatz, S. Mossmer, C. Hartmann, M. Moller, T. Herzog, M. Krieger, H.G. Boyen, P. Ziemann, B. Kabius, Langmuir 16 (2000) 407.
[21] S. Zou, R. Hong, T. Emrick, G.C. Walker, Langmuir 23 (2007) 1612.
[22] X. Li, H. Yang, L. Xu, X. Fu, H. Guo, X. Zhang, Macromol. Chem. Phys. 211 (2010) 297.
[23] T. Lohmueller, D. Aydin, M. Schwieder, C. Morhard, I. Louban, C. Pacholski, J.P. Spatz, Biointerphases 6 (2011) MR1.
[24] S. Mossmer, J.P. Spatz, M. Moller, T. Aberle, J. Schmidt, W. Burchard, Macromolecules 33 (2000) 4791.
[25] S. Papp, L. Korosi, B. Gool, T. Dederichs, P. Mela, M. Moller, I. Dekany, J. Therm. Anal. Calorim. 101 (2010) 865.
[26] S.T. Selvan, J.P. Spatz, H.A. Klok, M. Moller, Adv. Mater. 10 (1998) 132.
[27] R. Glass, M. Arnold, E.A. Cavalcanti-Adam, J. Blummel, C. Haferkemper, C. Dodd, J.P. Spatz, New J. Phys. 6 (2004) 101.
[28] G. Mie, Ann. Phys. (Leipzig) 25 (1908) 377.
[29] L.M. Liz-Marzán, Mater. Today 7 (2004) 26.
[30] D. Boyer, P. Tamarat, A. Maali, B. Lounis, M. Orrit, Science 297 (2002) 1160.
[31] P.K. Jain, K.S. Lee, I.H. El-Sayed, M.A. El-Sayed, J. Phys. Chem. B 110 (2006) 7238.
[32] J.N. Anker, W.P. Hall, O. Lyandres, N.C. Shah, J. Zhao, R.P. van Duyne, Nat. Mater. 7 (2008) 442.
[33] H. Chen, X. Kou, Z. Yang, W. Ni, J. Wang, Langmuir 24 (2008) 5233.
[34] D. Eck, C.A. Helm, N.J. Wagner, K.A. Vaynberg, Langmuir 17 (2001) 957.
[35] K.L. Kelly, E. Coronado, L.L. Zhao, G.C. Schatz, J. Phys. Chem. B 107 (2003) 668.
[36] M.W. Knight, Y. Wu, J.B. Lassiter, P. Nordlander, N.J. Halas, Nano Lett. 9 (2009) 2188.
[37] A.I. Kuznetsov, A.B. Evlyukhin, M.R. Goncalves, C. Reinhardt, A. Koroleva, M.L. Arnedillo, R. Kiyan, O. Marti, B.N. Chichkov, ACS Nano 5 (2011) 4843.
[38] J.B. Lassiter, M.W. Knight, N.A. Mirin, N.J. Halas, Nano Lett. 9 (2009) 4326.
[39] N. Nath, A. Chilkoti, Anal. Chem. 74 (2002) 504.
[40] Y.W.C. Cao, R.C. Jin, C.A. Mirkin, Science 297 (2002) 1536.
[41] T.J. Davis, K.C. Vernon, D.E. Gomez, Phys. Rev. B 79 (2009) 155423.
[42] W. Rechberger, A. Hohenau, A. Leitner, J.R. Krenn, B. Lamprecht, F.R. Aussenegg, Opt. Commun. 220 (2003) 137.
[43] S. Schultz, D.R. Smith, J.J. Mock, D.A. Schultz, Proc. Natl. Acad. Sci. USA 97 (2000) 996.
[44] I.E. Sendroiu, S.F.L. Mertens, D.J. Schiffrin, Phys. Chem. Chem. Phys. 8 (2006) 1430.
[45] K.H. Su, Q.H. Wei, X. Zhang, J.J. Mock, D.R. Smith, S. Schultz, Nano Lett. 3 (2003) 1087.
[46] P.K. Jain, W. Huang, M.A. El-Sayed, Nano Lett. 7 (2007) 2080.
[47] S.L. Altmann, Band Theory of Solids: An Introduction from the Point of View of Symmetry, Oxford University Press, New York, 1991.
[48] G. Kastle, H.G. Boyen, F. Weigl, G. Lengl, T. Herzog, P. Ziemann, S. Riethmuller, O. Mayer, C. Hartmann, J.P. Spatz, M. Moller, M. Ozawa, F. Banhart, M.G. Garnier, P. Oelhafen, Adv. Funct. Mater. 13 (2003) 853.
[49] S. Link, M.A. El-Sayed, J. Phys. Chem. B 103 (1999) 4212.
[50] K.R. Brown, M.J. Natan, Langmuir 14 (1998) 726.
[51] K.R. Brown, D.G. Walter, M.J. Natan, Chem. Mater. 12 (2000) 306.
[52] M. Brust, M. Walker, D. Bethell, D.J. Schiffrin, R. Whyman, J. Chem. Soc. Chem. Commun. (1994) 801.
[53] A. Henglein, Langmuir 15 (1999) 6738.
[54] N.R. Jana, L. Gearheart, C.J. Murphy, Langmuir 17 (2001) 6782.
[55] M.N. Martin, J.I. Basham, P. Chando, S.-K. Eah, Langmuir 26 (2010) 7410.
[56] J. Rodríguez-Fernández, J. Pérez-Juste, F. J. G. de Abajo, L.M. Liz-Marzán, Langmuir 22 (2006) 7007.
[57] J. Turkevich, P.C. Stevenson, J. Hillier, Discuss. Faraday Soc., 11 (1951) 55.
[58] C. Ziegler, A. Eychmueller, J. Phys. Chem. C 115 (2011) 4502.
[59] http://www.us.schott.com/advanced_optics/english/products/optical-materials/thin-glass/cover-glass-d-263-m/index.html.
[60] P.B. Johnson, R.W. Christy, Phys. Rev. B 6 (1972) 4370.
[61] E.D. Palik, Handbook of Optical Constants of Solids, Academic Press, Boston, 1997.
[62] J. Rheims, J. Koser, T. Wriedt, Meas. Sci. Technol. 8 (1997) 601.
[63] A. Samoc, J. Appl. Phys. 94 (2003) 6167.
[64] D.J. Segelstein. The Complex Refractive Index of Water. Thesis, University of Missouri, kansas Citry, 1981.
[65] V. Myroshnychenko, J. Rodríguez-Fernández, I. Pastoriza-Santos, A.M. Funston, C. Novo, P. Mulvaney, L.M. Liz-Marzán, F.J.G. de Abajo, Chem. Soc. Rev. 37 (2008) 1792.
[66] M. Quinten, U. Kreibig, Appl. Opt. 32 (1993) 6173.
[67] B.C. Sih, M.O. Wolf, J. Phys. Chem. B 110 (2006) 22298.
[68] G.D. Boreman, T. Johnson, A.C. Jones, S.-H. Oh, R.L. Olmon, M.B. Raschke, D. Shelton, B. Slovick, Broadband Electrical Permittivity of Gold for Plasmonics and Nano-Optics Applications, IEEE, New York, 2011.
[69] S. Underwood, P. Mulvaney, Langmuir 10 (1994) 3427.
[70] U. Kreibig, J. Phys. F: Met. Phys. 4 (1974) 999.
[71] P.K. Jain, X. Huang, I.H. El-Sayed, M.A. El-Sayed, Acc. Chem. Res. 41 (2008) 1578.
[72] U. Kreibig, M. Volmer, Optical Properties of Metal Clusters, Springer Verlag, Berlin, 1995.
[73] S. Link, M.A. El-Sayed, Int. Rev. Phys. Chem. 19 (2000) 409.
[74] W.P. McConnell, J.P. Novak, L.C. Brousseau, R.R. Fuierer, R.C. Tenent, D.L. Feldheim, J. Phys. Chem. B 104 (2000) 8925.
[75] C.F. Bohren, D.R. Huffman, Absorption and Scattering by Small Particles, Wiley, New York, 1983.
[76] W. Huang, W. Qian, M.A. El-Sayed, Y. Ding, Z.L. Wang, J. Phys. Chem. C 111 (2007) 10751.
[77] M.A.K. Abdelhalim, M.M. Mady, M.M. Ghannam, J. Nanomed. Nanotechnol. 3 (2012) 1000133.
[78] S. Link, M.A. El-Sayed, J. Phys. Chem. B 103 (1999) 8410.
[79] M.D. Malinsky, K.L. Kelly, G.C. Schatz, R.P. van Duyne, J. Am. Chem. Soc. 123 (2001) 1471.